Nationaal Lucht- en Ruimtevaartlaboratorium

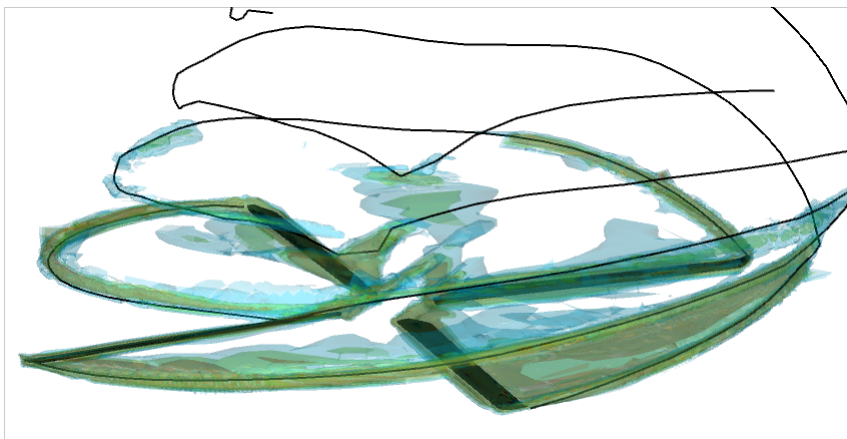National Aerospace Laboratory NLR

Executive summary

High-order simulation of a rotor in forward flight using a four-dimensional adaptive flow solver

Problem area

The simulation of rotorcraft aerodynamics is considerably more complex than the simulation of fixed wing aircraft aerodynamics. Rotorcraft flow is inherently dynamic, the inertial and elastic forces of the rotor blades interact with the aerodynamic forces, and aerodynamic interference of the rotor wake with the fuselage and tail rotor is important in many flight conditions.

The flow condition known as Blade-Vortex Interaction (BVI) is an important example of such interactions. Especially in low-speed descent, the rotor blades fly in their own wake. The (parallel) interaction of tip vortices and rotor blades causes strong pressure fluctuations on the blade,

responsible for the typical 'wopwop' sound of helicopters. Prediction of BVI is challenging: the blade motion under inertial, elastic, and aerodynamic forces must be predicted correctly and the convection of the tip vortices must be accurate enough to retain the vortices for, typically, one and a half rotor revolution (corresponding to a distance of one hundred blade chords).

This multiscale behaviour and multidisciplinary nature of rotorcraft aerodynamics has delayed the introduction of CFD techniques for rotorcraft aerodynamics. The numerical dissipation of standard CFD algorithms may destroy the vortex before the BVI event takes place. More advanced CFD algorithms, using high order

This report is based on a presentation held at the 34th European Rotorcraft Forum, Liverpool, UK, 16-18 September, 2008. Revision August 2009 based on new simulations

discretization and/or local grid refinement, are better suited to tackle the problem.

Description of work
In this paper, a high-order, adaptive flow solver is applied for the simulation of an isolated rotor at high speed. At such a speed, the wake still plays an important role in the vibratory loading of the hub, but the tip vortices convect more quickly outside the rotor disk area than in the low speed case. This renders the simulation more feasible on the current compute servers of NLR. This case is considered as a stepping stone towards the simulation of BVI. As such, special attention is paid to capture the blade-vortex interaction. Simulation results are compared with the corresponding experiment from the Helishape database.

Results and conclusions
The pre-adaptation strategy based on streak lines of particles released at the blade tips is effective and efficient in terms of grid size. The dynamic blade pressures compare well with experiment. The blade-vortex interaction in the experiment is weak. In the simulations, the effect of the increased vortex resolution does not have significant effects on the blade pressures, which is consistent with the experiment.

Applicability
The algorithm can be used to predict complex and localised phenomena occuring in rotorcraft aerodynamics, such as BVI.

NLR-TP-2008-696

High-order simulation of a rotor in forward flight using a four-dimensional adaptive flow solver
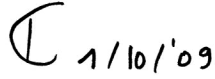
H. van der Ven and O.J. Boelens

The contents of this report may be cited on condition that full credit is given to NLR and the authors.

This publication has been refereed by the Advisory Committee AEROSPACE VEHICLES.

Customer	NLR/EU
Contract number	----
Owner	NLR
Division NLR	Aerospace Vehicles
Distribution	Unlimited
Classification of title	Unclassified
	September 2009

Approved by:

Author	Reviewer	Managing department
2009/9/29	29/09/09	1/10/'09

Summary

The accurate simulation of the rotor wake using first-principles based CFD is primarily a gridding problem. In order to capture the tip vortices the computational mesh must be refined in the vortex regions, which are not known beforehand and change position over time. In this paper, a high-order Discontinuous Galerkin method is combined with a pre-adaptation scheme on four-dimensional space-time meshes. An iterative pre-adaptation scheme is proposed, where the mesh is first refined on blade tip trajectories, and subsequently on streak lines of particles released at the blade tip. The streak lines are computed based on the flow solution obtained on the previous mesh. The algorithm is applied to the isolated 7AD1 rotor in high-speed flight. Comparison with experiment is favourable. The effectiveness of the pre-adaptation strategy combined with high-order simulation is demonstrated.

Contents

1 Introduction

In level helicopter flight there are two regimes with high vibration levels, low speed transition flight and high speed forward flight. The two high vibration regimes translate directly into high operating and maintenance costs (Datta et al. [2]). There are three key aerodynamic phenomena which contribute to the vibratory loads: wake induced airloads, compressibility effects, and dynamic stall. The current paper is focused on the accurate resolution of wake-induced airloads using Computational Fluid Dynamics (CFD) techniques.

The physics of rotor wakes has been discussed by various authors (see for example Conlisk [3] and McCroskey [10]). As summarised by Datta et al. [2], first principles CFD calculation of the wake is primarily a grid refinement problem. In order to capture the tip vortices the computational mesh must be refined in the vortex regions, which are not known beforehand. The dynamic nature of the wake in forward flight complicates the refinement problem since the vortices change position over time.

In recent years, the Netherlands National Aerospace Laboratory NLR has developed the four-dimensional MTMG algorithm for accurate rotor simulation. The algorithm is especially designed for those flight conditions where the detailed resolution of the wake is of the utmost importance [17], [7], [16]. The main design principle is to attain efficiency in the number of degrees of freedom, while maintaining a scalable algorithm on parallel machines. The aerodynamic CFD module in the algorithm demonstrates good vortex capturing capabilities, using local mesh refinement in both space and time, for relatively short turnaround times. A drawback of the method is its high memory requirement. For the simulation of a BO105 in BVI conditions it turns out that the resolution required to track the tip vortex for one and a half rotor revolution was unattainable using NLR's computing resources.

High order methods in principle have the capability of resolving the vortex with less degrees of freedom than conventional schemes. Hariharan and Sankar [5] have demonstrated that a 7th order ENO scheme is capable of capturing the tip vortex over 1-2 revolutions using only five points across the vortex core. The drawback of an ENO scheme is its non-local character, making it difficult to combine with a local mesh refinement algorithm. Discontinuous Galerkin (DG) methods [1] do not have that drawback: in principle, arbitrarily high-order schemes can be constructed on locally refined meshes with hanging nodes.

In this paper the higher-order DG method is applied to the simulation of a trimmed isolated rotor with elastic blades in high-speed flight. The outline of the paper is as follows: in the next

section the numerical method is briefly described. In Section 3 the high-speed test case is described. Section 4 describes the grid adaptation strategy for shocks and vortex wake, illustrated by the actual grid used in the simulation. Flow simulation results are presented in Section 5. Finally, in Section 6 conclusions are drawn.

2 Numerial method

The numerical method is a high-order DG scheme combined with an efficient space-time solver MTMG for time-periodic problems.

2.1 Multi-time multi-grid algorithm

The basic idea of the multi-time multi-grid (MTMG) [17] algorithm is that a time-periodic problem can be considered a steady problem in the sense that after one time period the next period shows the same physical phenomena. This is formalised by solving the time-dependent equations simultaneously in both space and time for the complete period of the problem. This is contrary to the usual time-serial approach, where one proceeds time step after time step on spatial grids. Now the time-dependent equations are solved on a four-dimensional space-time grid which contains all time levels in a period. Apart from generating a periodic solution by construction, the most relevant advantage for rotor simulations is that the time-accurate coupling of different physics models is straightforward. Another important benefit is that local grid refinement can be applied in space and time, while maintaining a scalable algorithm on massively parallel machines.

The current algorithm contains four modules, an aerodynamic module for the solution of the flow equations, a mesh refinement module to improve vortex resolution in the flow domain, an elastic module to account for the elastic blade deformations, and a trim module to trim the rotor system.

2.2 Discontinuous Galerkin finite element method

The compressible Euler equations of gas dynamics are solved using the discontinuous Galerkin (DG) finite element method in an arbitrary Lagrangian-Eulerian formulation to accommodate moving meshes. Details of the flow solver can be found in Van der Vegt et al. [12]. Of particular relevance for the simulation of vortex flow is the fact that the DG method not only solves for cell-averaged flow data, but also for the flow gradients. The flow gradients are used to determine the vorticity directly and as such vorticity transport is contained in the discrete equations. Moreover, the DG method is ideally suited for local grid refinement.

The flow gradients are part of the numerical scheme by combining constant basis functions within each element with linear basis functions. An obvious extension to the scheme is to allow quadratic or cubic basis functions. This effectively increases the order of accuracy of the scheme to three or four. The drawback is that the number of degrees of freedom per element is also increased. In one dimension, the second order scheme has two degrees of freedom per element, the third order scheme has three, and the fourth order scheme has four. In higher dimensions, the increase in the number of degrees of freedom is more dramatic: the second order scheme in four dimensions has five degrees of freedom per element, third order 15, and fourth order 35. In this paper, the third order scheme will be applied, and compared with the second order scheme.

As shown above, the third order scheme solves three times as many unknowns as the second order scheme. For the stepping-stone test case of 2D vortex convection it has been found that the third order method has the same resolution characteristics as the second order method on a mesh which is once refined in every direction. For four-dimensional simulations such a uniformly refined mesh contains 16 times more grid points, so it is expected that the third order scheme is 16/3 times more efficient than the second order scheme.

3 Test case

Data point 135 of the Helishape wind tunnel program is simulated [12]. This data point concerns a high-speed level flight case at an advance ratio of 0.356 for the isolated 7AD1 rotor with parabolic and anhedral tip. The blade has a radius R of 2.1m and a chord c of 0.14m (aspect ratio R/c=15). In the experiment the rotor is trimmed for a thrust coefficient of C_T=0.0071 and zero flapping.

The flow displays (weak) shocks at the advancing side and the vortex wake contributes to the vibratory loads at the rotor hub. Hence a CFD mesh must be generated capable of resolving shocks and vortices.

4 Adaptation strategy

For industrial applications the most common grid adaptation strategy is to use sensors based on flow features. Shock sensors based on gradients in the flow have in general been quite effective

in resolving shocks. For tip vortices in the rotor wake the effectiveness of feature-based sensors is not so clear. The straightforward vorticity magnitude sensor does not discriminate between tip vortices, vortex sheets or numerically induced boundary layers. More advanced sensors, such as the λ_2 criterion (Jeong et al. [7]), require significant resolution of the vortex to detect it. Such a resolution is not present on the initial coarse meshes. Because of these findings, it was concluded to opt for pre-adaptation, where the mesh is refined before the actual flow computation, based on the expected location of the tip vortices. This will be explained in detail later. In effect, the pre-adaptation strategy resembles unstructured grid generation more than conventional mesh refinement. It is comparable to the Chimera approach of Dietz et al. [5], where Chimera grids are constructed around the expected tip vortex locations. The benefit of our approach is that it is still based on the single-grid concept.

4.1 Relevant scales

Since we solve the Euler equations there is no physical limit to the vortex strength. Under mesh refinement the tip vortices will grow stronger and stronger. In order to avoid excessive grid refinement, the cell diameters should be limited from below. The minimal cell diameter is in general set to $R/200$, which is one quart of the experimentally determined vortex core size, where R is the rotor radius (Caradonna, [2]). Roughly speaking, this resolution corresponds to 12 degrees of freedom in each direction in the vortex core for the third-order DG method.

In order to avoid dispersion of the vortex in time, the physical time step in the vortex should correspond to a CFL number $u\Delta t / \Delta x$ of the order of one. The reference velocity is the magnitude of the freestream velocity. Note that we have taken the CFL number corresponding to the convective velocity and not the acoustic signals, since the main mechanism in the wake is convection of vorticity. Let T be the period of one revolution, then the time step restriction translates to the following relation:

$$\frac{\Delta t}{T} = \frac{\Delta x}{uT} = \frac{\Delta x}{2\pi R}\frac{\Omega R}{u} = \frac{\Delta x/R}{2\pi\mu}$$

where μ is the advance ratio. With $\Delta x / R = 1/200$, an advance ratio of 0.35 we need about four hundred time steps for one revolution, or one hundred for one period of a four-bladed rotor, corresponding to an increment of less than one degree azimuth. Note that this time step should be sufficient for the convection of the vortex, but not necessarily for blade-vortex interaction.

4.2 Pre-adaptation on blade geometry

For the four-dimensional algorithm it is of the utmost importance to be efficient in the number of grid points. Using the pre-adaptation strategy as a kind of grid generation, the starting grid should be as coarse as possible. At NLR, the starting grid is generated using a multi-block structured grid generator. In a block-structured grid, the resolution required at the geometry will

extend into the flow domain. In order to reduce the number of elements, a coarse mesh is generated, which is subsequently locally refined near the blades. Care is taken that the blade geometry is well-represented under local refinement. An impression of the resolution of the resulting mesh is shown in Figure 1. The number of elements is 64 in the chord direction and 104 in the span direction. Subsequently, the mesh has been refined using the standard shock sensor to increase the (weak) shock resolution at the advancing side (Figure 2).

The space-time mesh obtained using this geometry refinement is referred to as Mesh G0. It contains 12.3 million elements, distributed over 64 time levels, which is in the order of the 100 time levels required for vortex convection. The blade motion has been trimmed on this mesh, taking into account elastic blade deformations.

4.3 Pre-adaptation on blade tip trajectories

By their nature, the location of the tip vortices is predominantly determined by the trajectory of the tip. So, to a very good approximation, the vortex trajectories can be taken to be the blade tip trajectories. The blade tip trajectories $\Gamma(t)$ at time t are cycloids, described by

$$\Gamma(t) = \left\{ \left(R\cos(\Omega(t-s)), R\sin(\Omega(t-s), w(t-s)) + \vec{u}_\infty s \mid s \geq 0 \right\},$$

where Ω is the rotor frequency, $w=w(t)$ is the flapping motion of the tip, and $\vec{u}_\infty$ is the free stream velocity.

Based on this geometrical information, the mesh may be pre-adapted to increase the resolution near the tip trajectories. Whenever a cell is within a given distance of a tip trajectory and the mesh width or the time step is greater than a given threshold the cell is refined. Eventually a mesh is 'generated' with uniform space-time resolution in the expected vortex regions. The main benefit of this method is that there will be no refinement in other regions, for instance in the vortex sheets, hence the total number of grid cells is reduced compared to feature-based adaptation.

4.4 Pre-adaptation on streak lines

Of course, the assumption that the tip vortices follow the tip trajectories ignores the effects of downwash, contraction and interaction. Hence the free stream velocity in the definition of the tip trajectories $\Gamma(t)$ is replaced by the actual, computed velocity field. That is, the blade tip trajectories are replaced by the streak lines of particles released at the blade tips.

In this way, an iterative pre-adaptive procedure is constructed, where the accuracy of the predicted tip vortex locations is increased with each iteration. In Figure 3 and Figure 4, a

comparison is made between the blade tip trajectories and the streak lines of particles released at the blade tips (using the flow results of the next section). The difference increases with the age of the vortex. The main difference between the two methods is that the second accounts for the downwash of the rotor.

Based on a high-order solution on a mesh obtained by pre-adaptation on the blade tip trajectories, streak lines are computed which are used for the next pre-adaptation. The next pre-adaptation is executed on Mesh G0, that is, the previous pre-adapted mesh is discarded. The mesh is generated in several adaptation steps, where each step zooms in on the expected vortex location by reducing both the target mesh width and the region in which the grid is refined. First the cells at a distance of $0.1R$ are refined with the target mesh width $0.02R$. Both distance and mesh width are decreased proportionally, and the final step in the adaptation process has a target mesh width of $0.007R$ at a distance of $0.035R$. The final mesh, labelled G1, has 17.3 million elements.

The 17.3 million elements of Mesh G1 are equivalent to 260 million degrees of freedom per equation. Since the space-time mesh contains 64 time slabs, the average number of degrees of freedom per time slab is 4 million. This clearly is a modest number when trying to resolve the rotor wake.

It should be remarked that the target mesh width is not necessarily attained. A cell is refined whenever the mesh width is more than two times the target mesh width. Hence, on the final mesh, mesh widths will be between once and twice the target mesh width. Moreover, out of practical considerations, the mesh adaptation is stopped before saturation of the refinement criterion, and the quality of the mesh is judged by inspection.

Figure 5 and Figure 6 show Mesh G1 at two horizontal cross sections. The expected tip vortex locations are shown as curves, and blanked when the distance of the curve to the plane is greater than $0.035R$, which is the user-defined distance within which cells should be refined. Figure 7 illustrates the pre-adaptation algorithm in a grid plane through the rotor axis and approximately perpendicular to the vortices.

It is clear from these figures that the mesh has been refined in a uniform way near the predicted vortex locations, and nowhere else. Hence the pre-adaptation algorithm is very effective in limiting the number of refined elements.

5 Flow results

In the experiment the rotor is trimmed for thrust, drag and zero flapping. The latter is not possible in our MTMG framework, so the rotor is trimmed for thrust and zero pitching and rolling moment. The resulting elastic deformation is shown in Figure 8. As can be seen the flapping (or bending) motion varies between 2 and 4% of the rotor radius; and hence the variation cannot be considered negligible.

In order to evaluate the effect of the different trimming the sectional normal force is analyzed. Sectional normal force as a function of the azimuth angle is presented in Figure 9 for five different span stations. Overall agreement with experiment is satisfactory. In the first quadrant the normal forces are comparable, in the next quadrant the simulation shows higher loadings, probably due to a larger angle of attack. This will be analyzed in detail when the pressure distributions are discussed. On the retreating side, the largest difference is at 50% span, where the experiment shows evidence of blade-vortex interactions, which are not visible in the simulation. As can be seen in Figure 10, the miss distance of a tip vortex with retreating blade at 315 degrees exceeds $0.1R$, which is too large to have noticeable effect on the sectional normal force. As both the position of the blade and the position of the tip vortices critically depend on the trim, the large miss distance in the simulation is most probably caused by the difference in the trim procedure. Based on this finding, we will concentrate on blade-vortex interactions at the advancing side, in the first quadrant.

Pressure distributions at selected stations and azimuth angles are compared with experimental data in Figure 11. Simulation results are obtained with the third order simulation on Mesh G1. There is hardly any difference with the second-order solution (not shown). General agreement is good. As is expected from the analysis of the sectional normal forces, the agreement in the first quadrant is very good; in the second quadrant the simulation shows pressure distributions which are consistent with a higher angle of attack than in the experiment. The resulting sectional lift will be larger, which is consistent with Figure 9.

Time histories of the pressure at selected blade stations are shown in Figure 12 (for the second order simulation) and Figure 13 (for the third order simulation). Of special interest are the stations near the leading edge at the lower side of the blade, which are the most sensitive to vortex interaction. Unfortunately, the blade-vortex interactions in the experiment are weak, and not always discernible from low pressure due to changes in angle of attack. For instance, the inverted peaks in Figure 12 (d) and (g) between azimuths 90 and 135 degrees cannot be due to blade vortex interactions since there are no vortices present at these radial locations and

azimuths. Moreover, a blade-vortex interaction is a short phenomenon, typically lasting three to five degrees azimuth. There is a blade-vortex interaction just before or at 90 degrees azimuth, which is clearly visible in the simulations at $r=0.92$ R (Figure 12(g)) and more weakly, in the third order solutions only, at $r=0.82$ R and 100 degrees (Figure 13 (d)). The same interaction at $r=0.7$ R is hardly visible (Figure 13 (a) at 120 degrees azimuth). The interactions quickly weaken further down the airfoil as is visible from the figures at 6% from the trailing edge. Finally, Figure 13(i) again shows that in the simulation the local angle of attack for azimuths greater than 90 degrees are greater than in the experiment.

The difference between the second order and third order discretization on the blade vortex interactions, is shown in detail in Figure 14 (2% from leading edge at $r=0.92$ R). The third order discretization clearly shows a stronger interaction (where the strength of the interaction is measured as the gradient of the pressure signal).

Figure 15 shows the vortex systems at an azimuth angle of 45 and 67.5 degrees, for second and third order solutions. Clearly, the second order simulations show little evidence of vortices at the shown vorticity levels: the vortices are present but weak. The third order solutions show much improvement over the second order solutions. The fact that the improved vortex persistence of the third order scheme shows little effect in the blade pressures, again demonstrates that the miss distance is quite large.

Figure 16 displays the vortex system, viewed from below, at an azimuth angle of 56 degrees for the third order simulation. Since the vortex wake is located below the rotor disk, this view presents a clear picture of the vortex system. At the retreating side (bottom of the figure), vortices of four different ages are visible. At the advancing side (top of the figure) only two vortices are visible. The advancing side vortices appear to be weaker and are destroyed by the root vortices at the hub.

In the following figures the vortex system is discussed in more detail. Each set of figures shows the vortex system from above (for example, Figure 18), and in a cross-sectional vertical slice (for instance, Figure 19 and Figure 20). The figure with the vortex system viewed from above also presents the location of the cross-sectional plane, including numbered labels at locations where the vortices intersect the plane. The numbers are repeated in figures of the cross-sectional slice, with an additional letter, signifying whether the vortex is a tip vortex ('T') of root vortex ('R').

In Figure 19, tip vortices of four ages are visible in the third order solution: T1, T2, T4, and T5. Note that these vortices are barely visible in the second order solution. Tip vortex T6 is the tip vortex with about the same age of vortex T1, and hence is much clearer. The root vortices R3 and R4 are located near the tip vortices T2 and T4, and since they are of opposite rotation they are likely to destroy the tip vortices. In reality the wake of the hub will have weaker interactional effects than the present root vortices. Comparing the vortex locations and grid resolution in Figure 20, shows that the grid has been refined in the correct locations.

Figure 23 shows the vortex system at a later stage and more on the advancing side of the rotor. The two tip vortices T1 and T2 are clearly visible in the third order simulation results, but the next tip vortex T3 is very weak. Note the different scale in the vorticity levels: the tip vortices emanating from the blades in the second quadrant are weaker than the vortices emanating from the blades in the third quadrant (compare Figure 19). As the blade loading is not significantly different for the two quadrants, this is most probably due by lack of resolution (see Figure 24).

Finally, two cross-sectional planes through the rotor blades are presented in Figure 26 at an azimuth angle of 80 degrees. The solution in the plane through the blades at 170° and 350° azimuth (Figure 27) shows a clear tip vortex T1, close to the blade, but further downstream the vortices are interacting with the root vortices R2 and R3. The solution in the plane through the blade at 80° azimuth (Figure 29) shows a clear vortex TI, but the next vortex TII has weakened and is located at a significant distance of the blade and will have little influence on the blade pressures.

For all the cross-sectional planes discussed above, the adaptation algorithm accurately refines the cells at the actual vortex locations (apart from the vortices emanating from the blade in the second quadrant, see Figure 30). In general one can conclude that the pre-adaptation on streak lines is an efficient and accurate way of generating meshes with sufficient resolution in the vortex regions.

6 Computational characteristics

The computational complexity of the simulation is as follows. The trim is executed on the coarse mesh without vortex refinement, and is negligible compared to obtaining the third-order solution on the vortex-refined mesh. Pre-adaptation of the mesh is executed in 12 steps, each of which takes about 10,000 CPU seconds on a single vector processor NEC SX8-R. Note that the adaptation algorithm is primarily a scalar algorithm. The total time for the pre-adaptation is hence about one and a half day. For the second order solution, 200 p-multigrid cycles with 5

pre- and post relaxations have been taken, which require 1.6 million CPU seconds. Running on three processors at a speed of 17 Gflop/s this takes six days. Memory use is 30 GB. For the third order solution, a subsequent 75 p-multigrid cycles with 5 pre- and post relaxations have been taken, which require 2.1 million CPU seconds. Running on three processors at a speed of 22 Gflop/s this takes eight days. Memory use is 57 GB.

Note that at a peak speed of 128 Gflop/s the NEC SX-8R/8 is a small compute server. Considering the scalability of the algorithm, the simulations described in this report are expected to take less than a day on a teraflop machine.

7 Conclusions

A comprehensive approach to the simulation of the rotor wake using first-principles CFD has been presented. The effectiveness of the pre-adaptation strategy for the vortex-convection for an isolated rotor in high-speed flight has been demonstrated. Given the differences in trimming procedure, the agreement with experiment is relatively good. The blade-vortex interaction at the advancing side in the experiment is weak. In the simulations, the effect of the increased vortex resolution does not have significant effects on the blade pressures, which is consistent with the experiment.

Acknowledgements
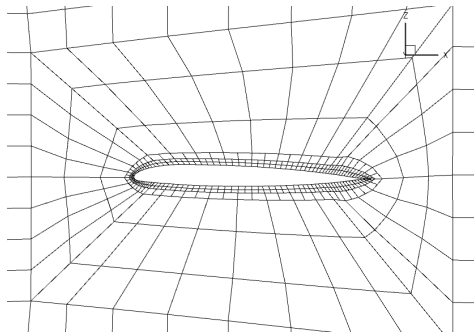
Figure 1 Blade cross section of the mesh after geometry refinement
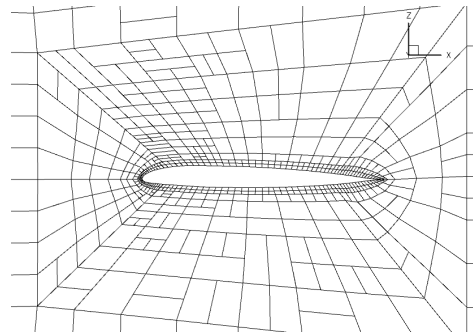
Figure 2 Same cross section after feature refinement
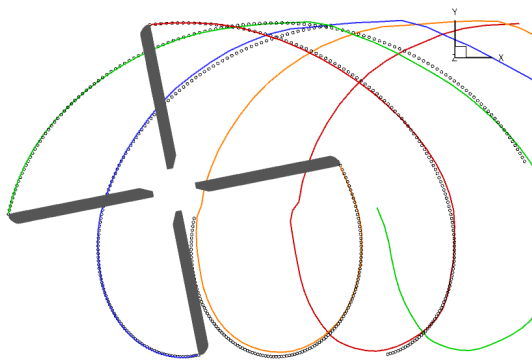
Figure 3 Difference between the blade tip trajectories and the predicted vortex locations using particle traces. Perpendicular view.
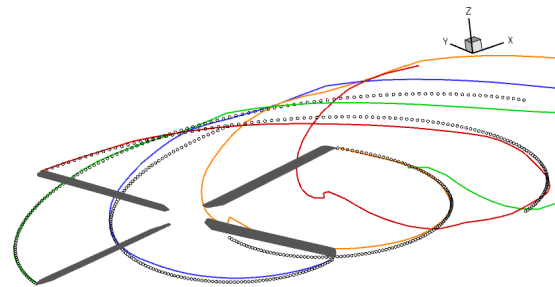
Figure 4 Difference between the blade tip trajectories and the predicted vortex locations using particle traces. Main difference is the effect of the downwash of the rotor.
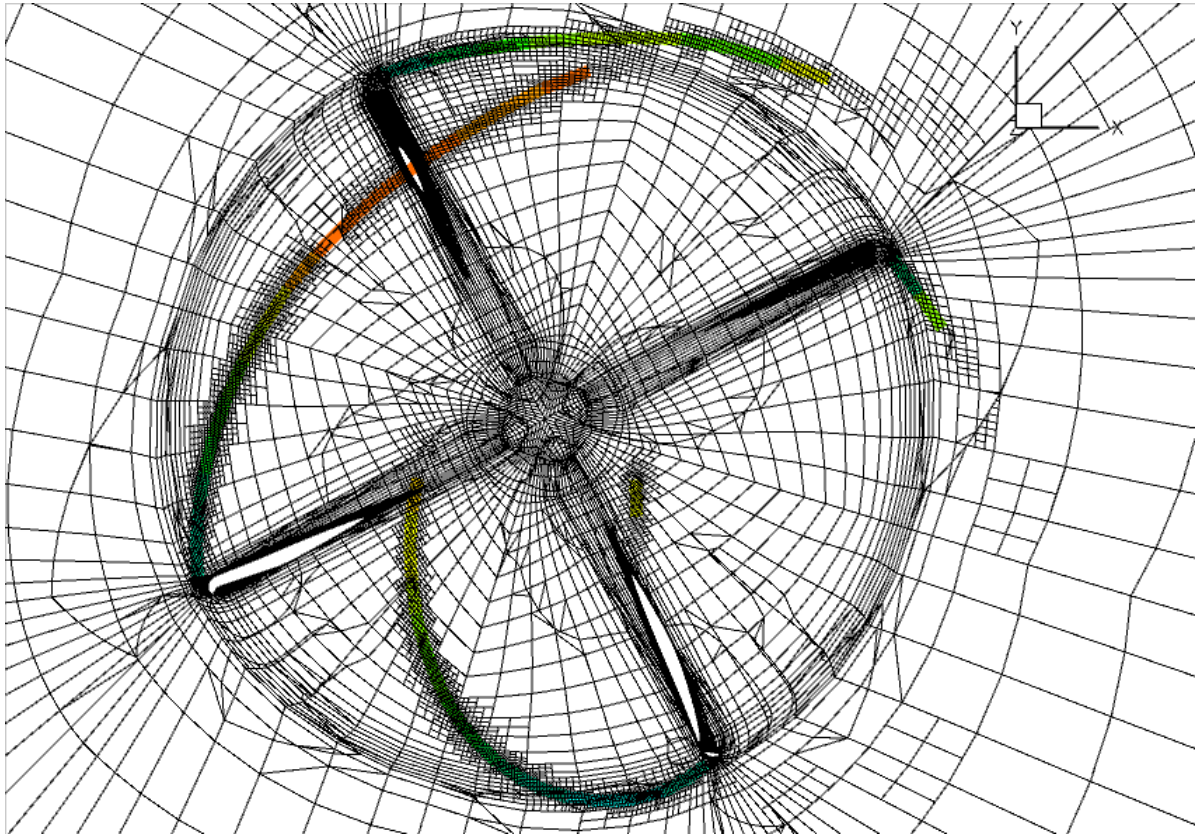
Figure 5 Illustration of the pre-adaptation strategy. An arbitrary horizontal slice of Mesh G3 is shown, together with the expected vortex locations as predicted by the particle traces. The vortex locations are coloured with their distance to plane, and not shown if the distance is greater than 0.0375R. Clearly visible is the refinement regions near the expected vortex locations.
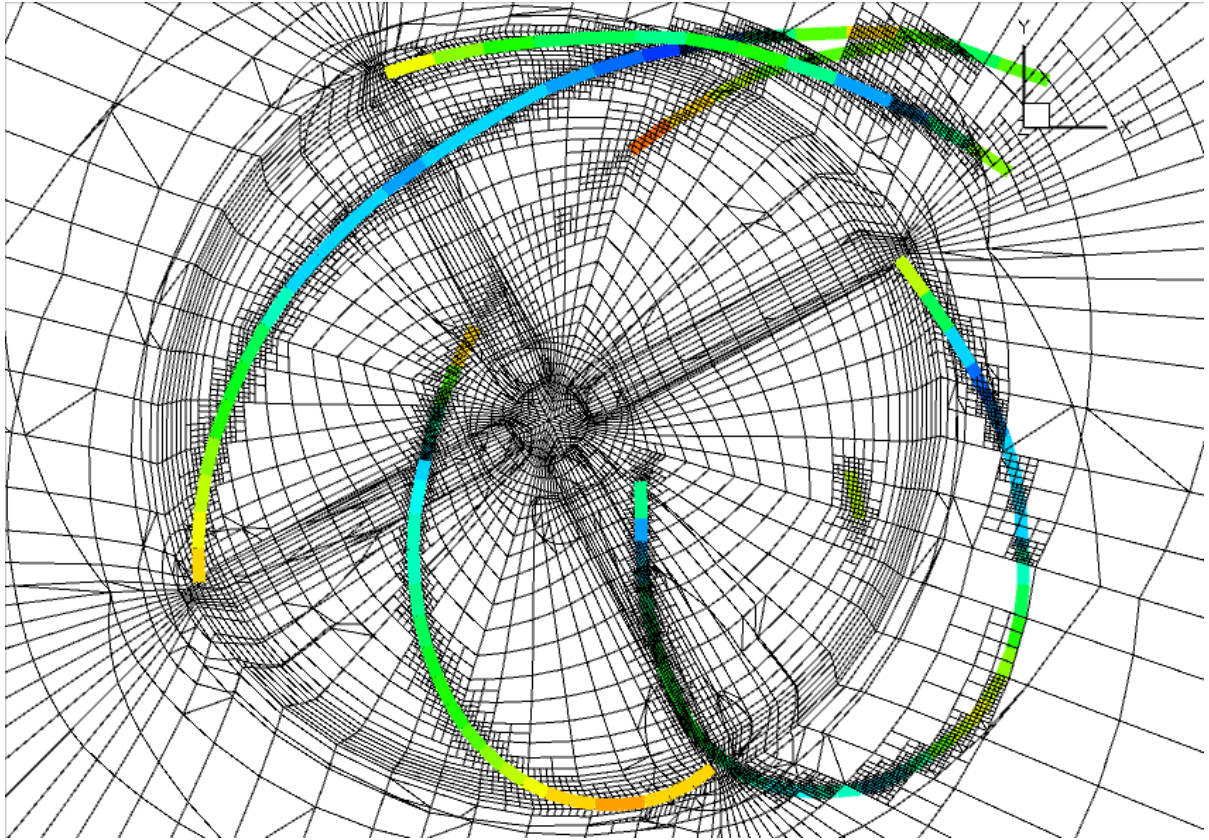
Figure 6 As the previous figure, but a different horizontal plane, below the previous one
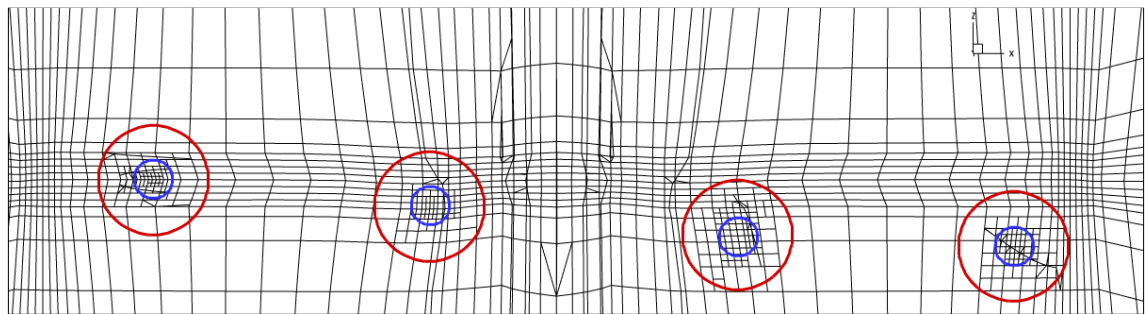
Figure 7 Impression of the mesh obtained from pre-adaptation on streak lines. The grid plane shown is through the rotor axis (in the center of the figure) and almost perpendicular to the vortices. The red circles have a diameter of 0.1R (within the circles the target mesh width 0.02R); the blue circles have a diameter of 0.035R (within the circles the target mesh width is 0.007R)
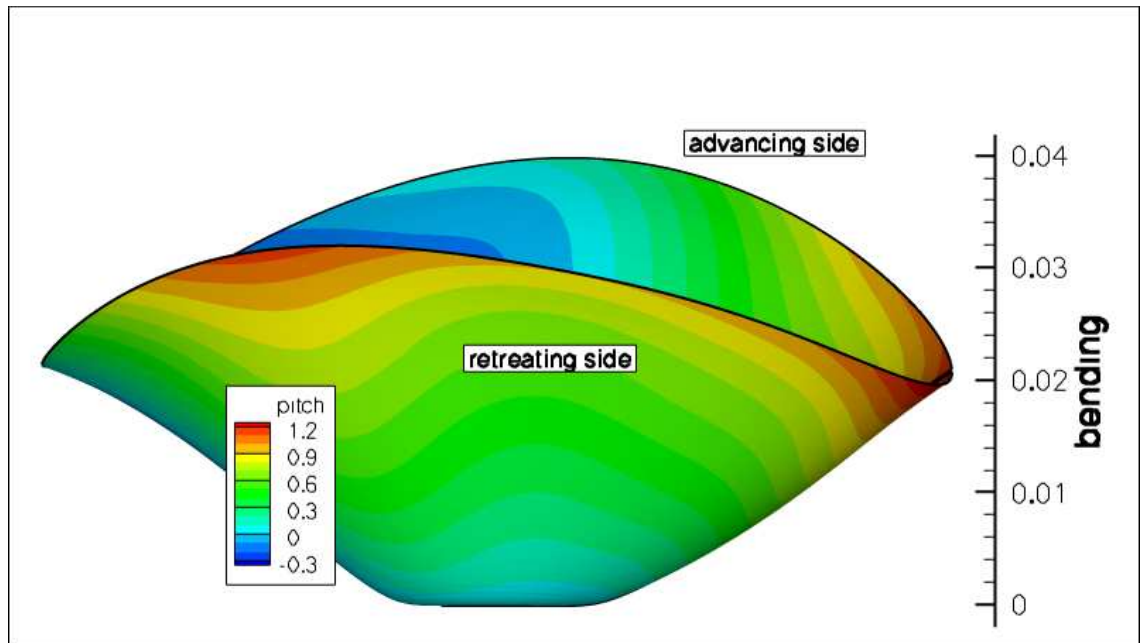
Figure 8 Representation of the elastic blade motion of the rotor disk. The elastic flap motion is visible as the bending (z-coordinate, in units of the rotor radius) and the rotor disk is coloured with the elastic pitch (in degrees).
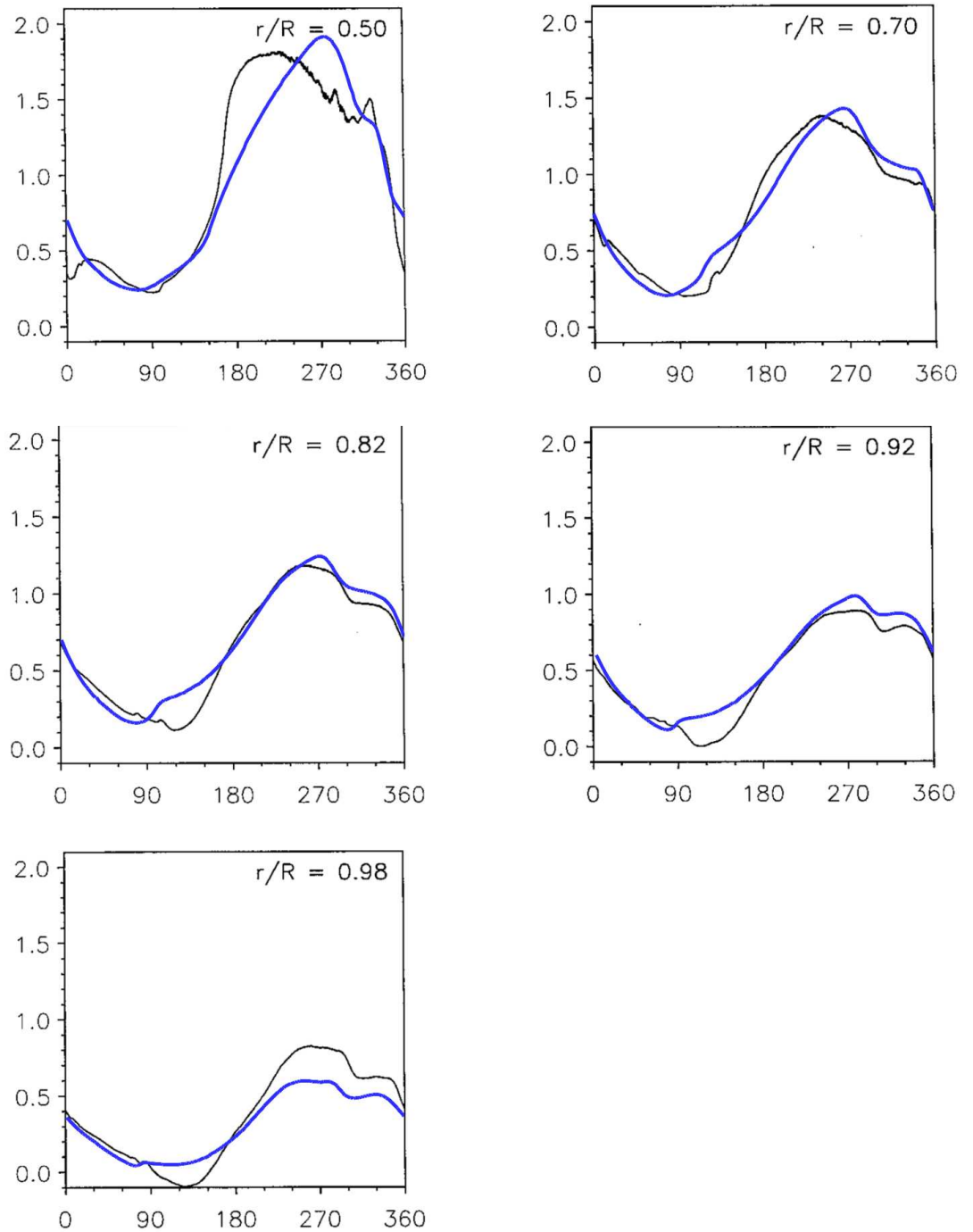
Figure 9 Sectional normal force coefficient as a function of azimuth at five spanwise stations. Black line: experiment; blue line: simulation. Third order simulation.
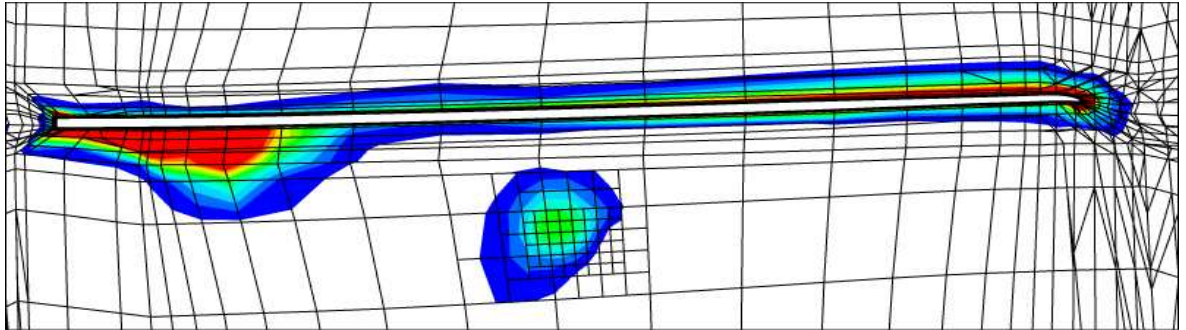
Figure 10 Miss distance of a blade tip vortex with a retreating blade at ψ=315°

(a) r/R=0.7, ψ=0°   *(b) r/R=0.7, ψ=90°*   *(c) r/R=0.7, ψ=270°*

(d) r/R=0.82, ψ=45°   *(e) r/R=0.82, ψ=90°*   *(e) r/R=0.82, ψ=120°*

(f) r/R=0.92, ψ=60°   *(g) r/R=0.92, ψ=90°*   *(h) r/R=0.92, ψ=120°*
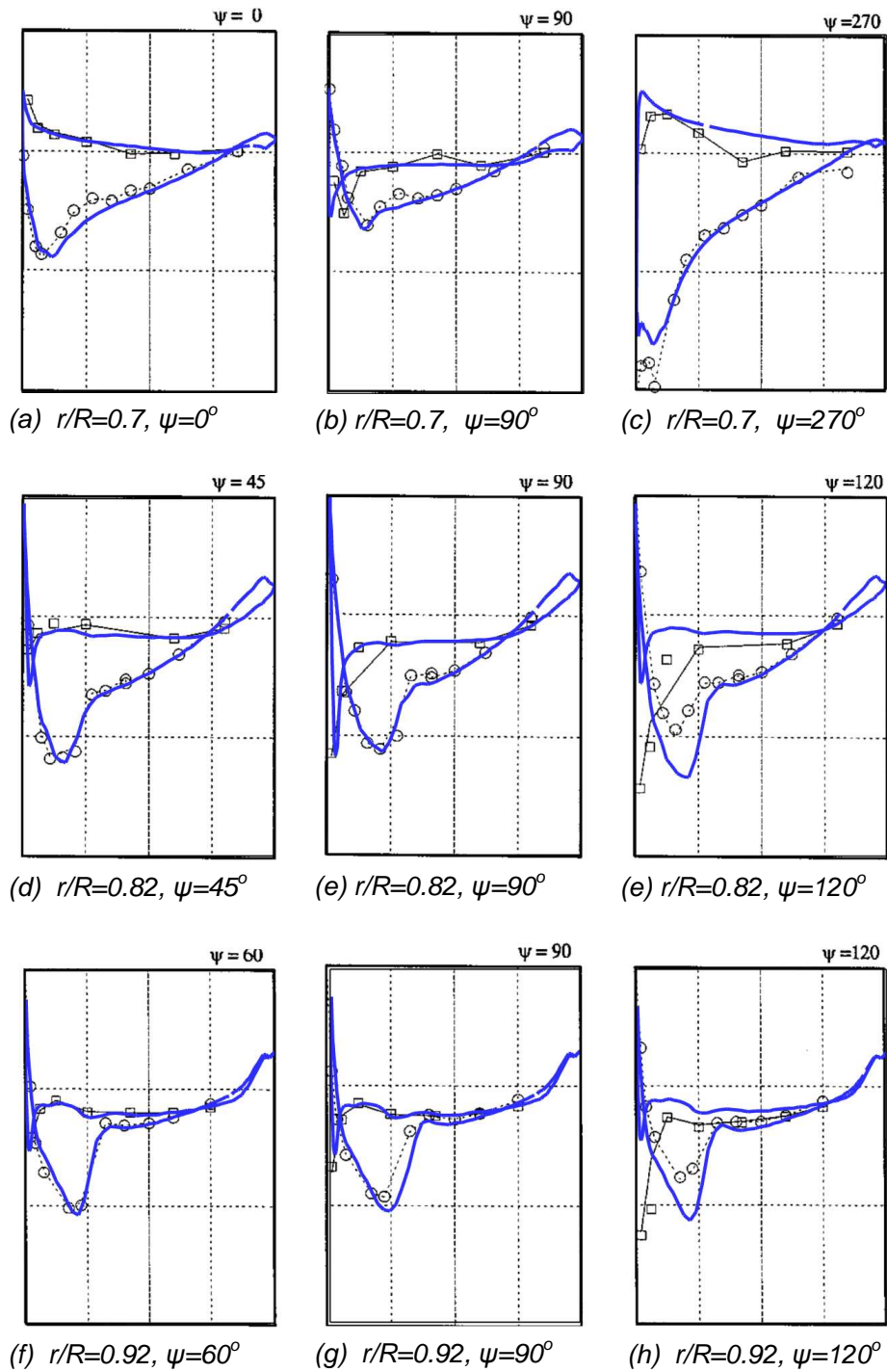
Figure 11 Pressure distributions at various span stations and azimuth angles. Lines with circles: experiment (dotted: upper side; solid: lower side). Solid blue line: simulation. Shown is the pressure against chordwise position. Third order simulation.

(a) r=0.7R, x/c=0.06 at lower side

(b) r=0.7R, x/c=0.35 at upper side

(c) r=0.82R, x/c=0.21 at upper side

(d) r=0.82R, x/c=0.02 at lower side

(e) r=0.82R, x/c=0.06 at lower side

(f) r=0.82R, x/c=0.02 at upper side

(g) r=0.92R, x/c=0.02 at lower side

(h) r=0.92R, x/c=0.06 at lower side

(i) r=0.92R, x/c=0.325 at upper side
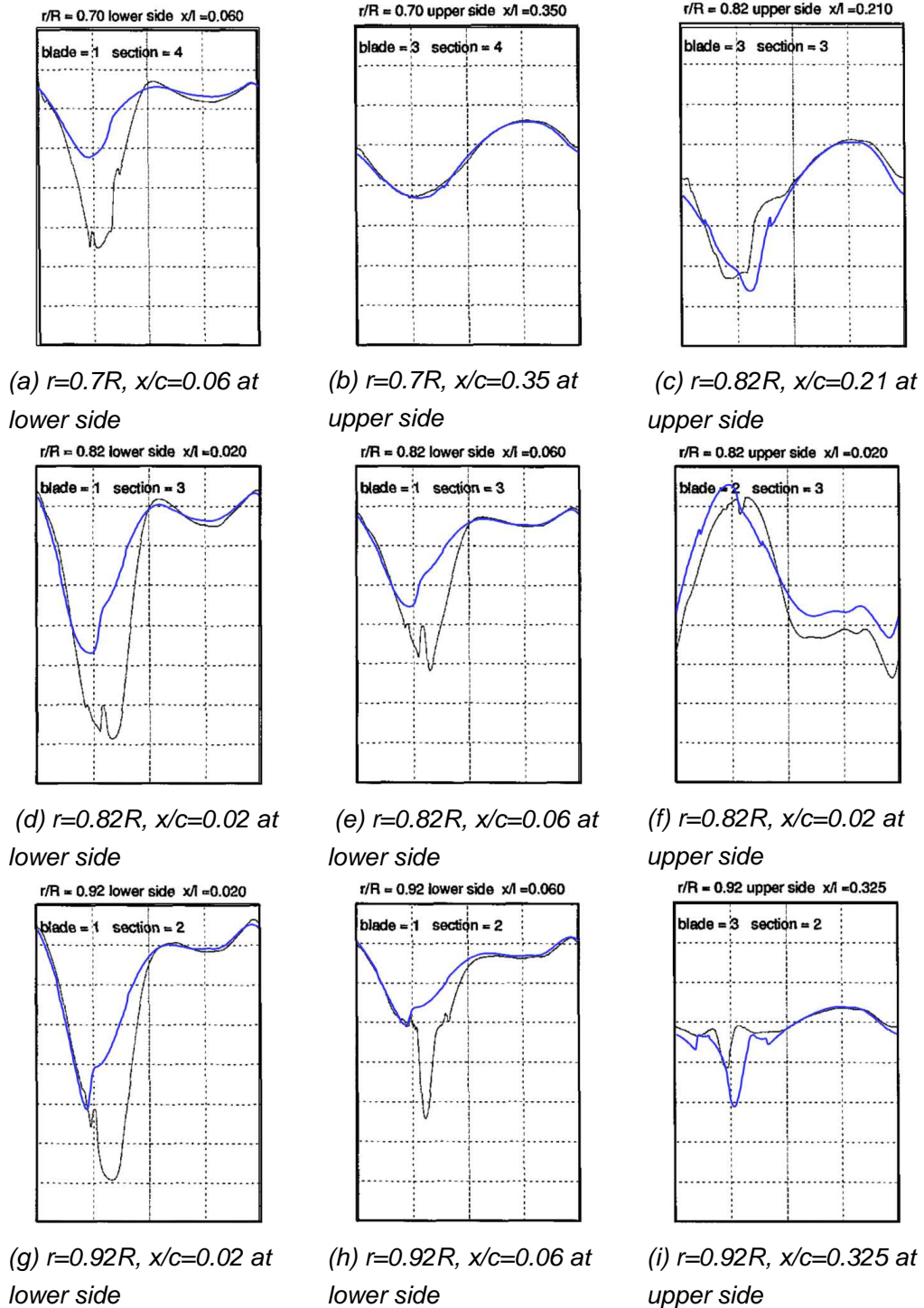
Figure 12 Pressure histories at selected stations on the blade. Solid black line: experiment. Solid blue line: simulation. Shown is the pressure against azimuth angle for one revolution. Second order simulation.

(a) r=0.7R, x/c=0.06 at lower side

(b) r=0.7R, x/c=0.35 at upper side

(c) r=0.82R, x/c=0.21 at upper side

(d) r=0.82R, x/c=0.02 at lower side

(e) r=0.82R, x/c=0.06 at lower side

(f) r=0.82R, x/c=0.02 at upper side

(g) r=0.92R, x/c=0.02 at lower side

(h) r=0.92R, x/c=0.06 at lower side

(i) r=0.92R, x/c=0.325 at upper side
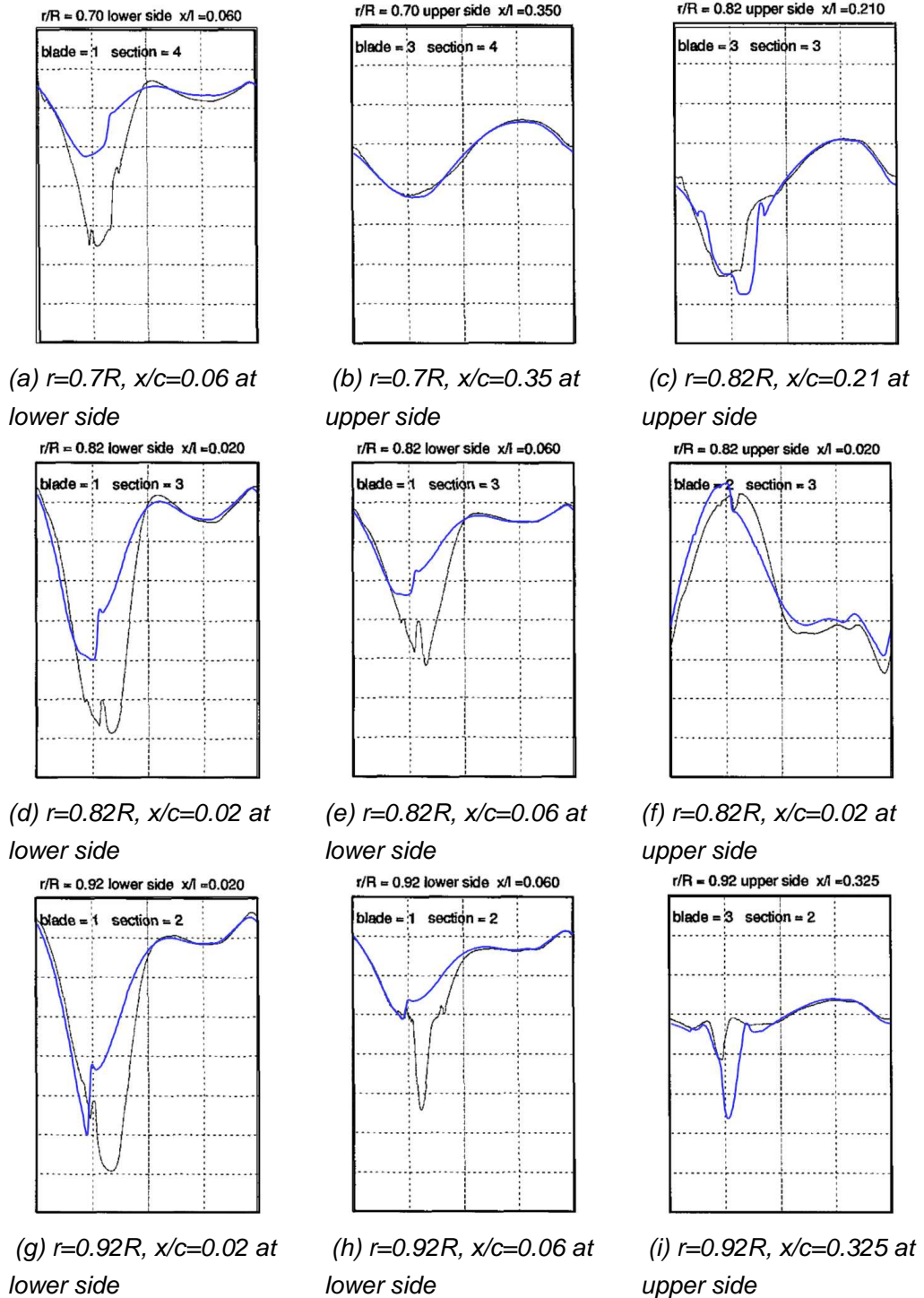
Figure 13 Pressure histories at selected stations on the blade. Solid black line: experiment. Solid blue line: simulation. Shown is the pressure against azimuth angle for one revolution. Third order simulation
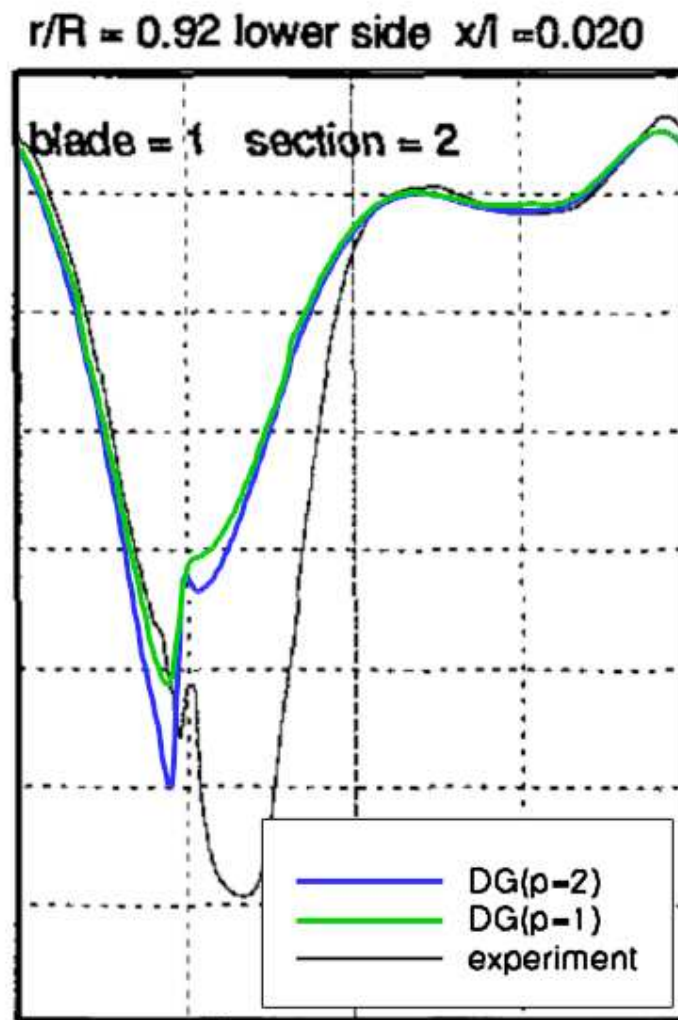
Figure 14 Comparison of time series of pressure at r/R=0.82 span station and x/c=0.06 chord station at the lower side. Red: Mesh G0, second order DG; Green: second order DG; Blue: third order DG.
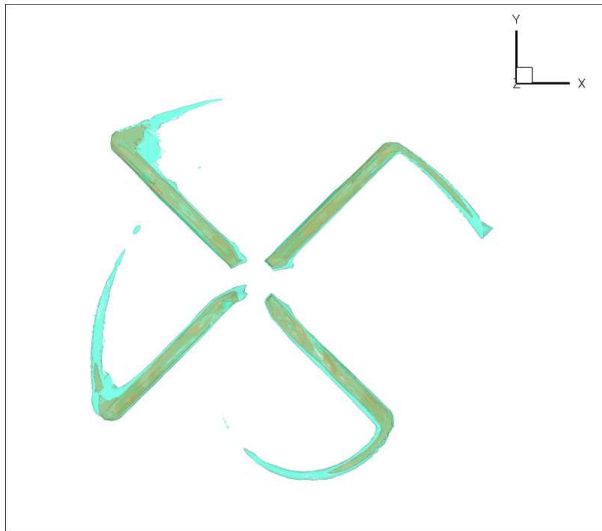
(a) second order at ψ=45°
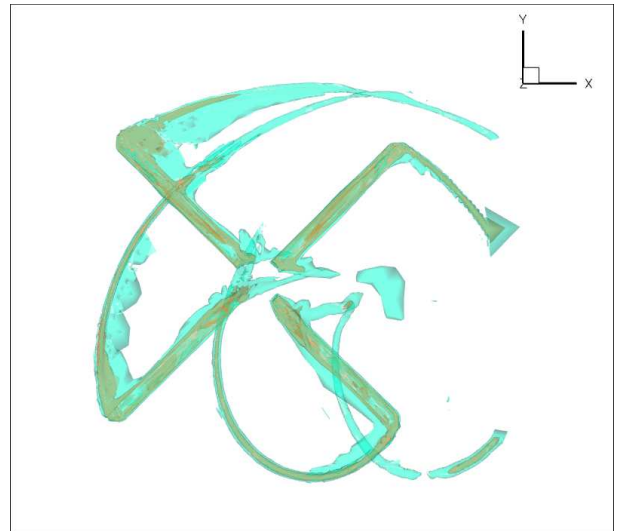
(b) third order at ψ=45°
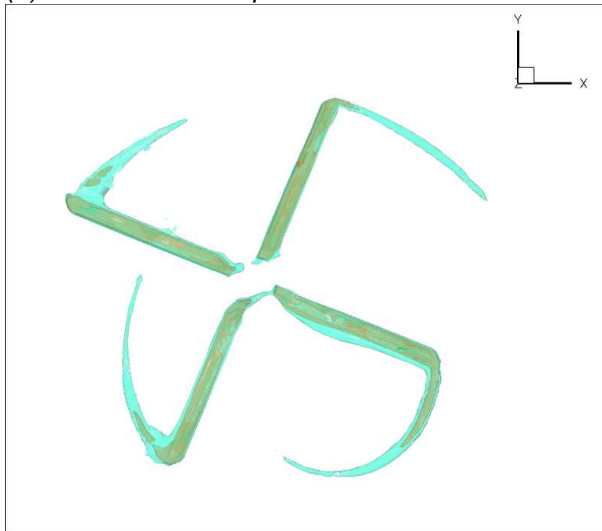
(c) second order at ψ=67.5°
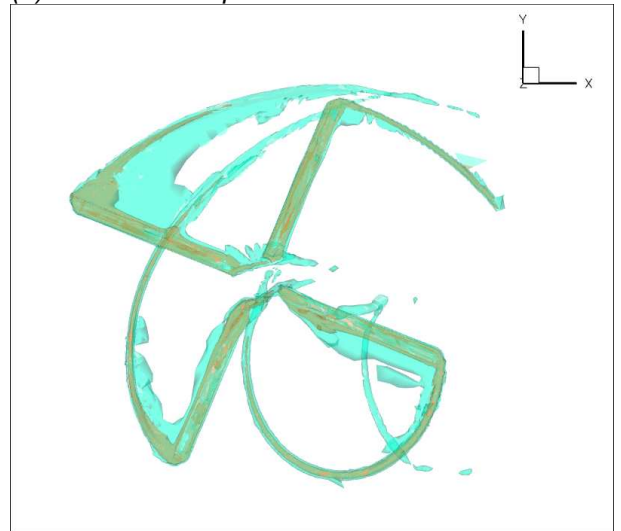
(d) third order at ψ=67.5°

Figure 15. Comparison of vorticity contours between order of accuracy. Iso-contours are shown at vorticity magnitude level of $2a_\infty/R$ and $5a_\infty/R$, where a_∞ is the speed of sound.
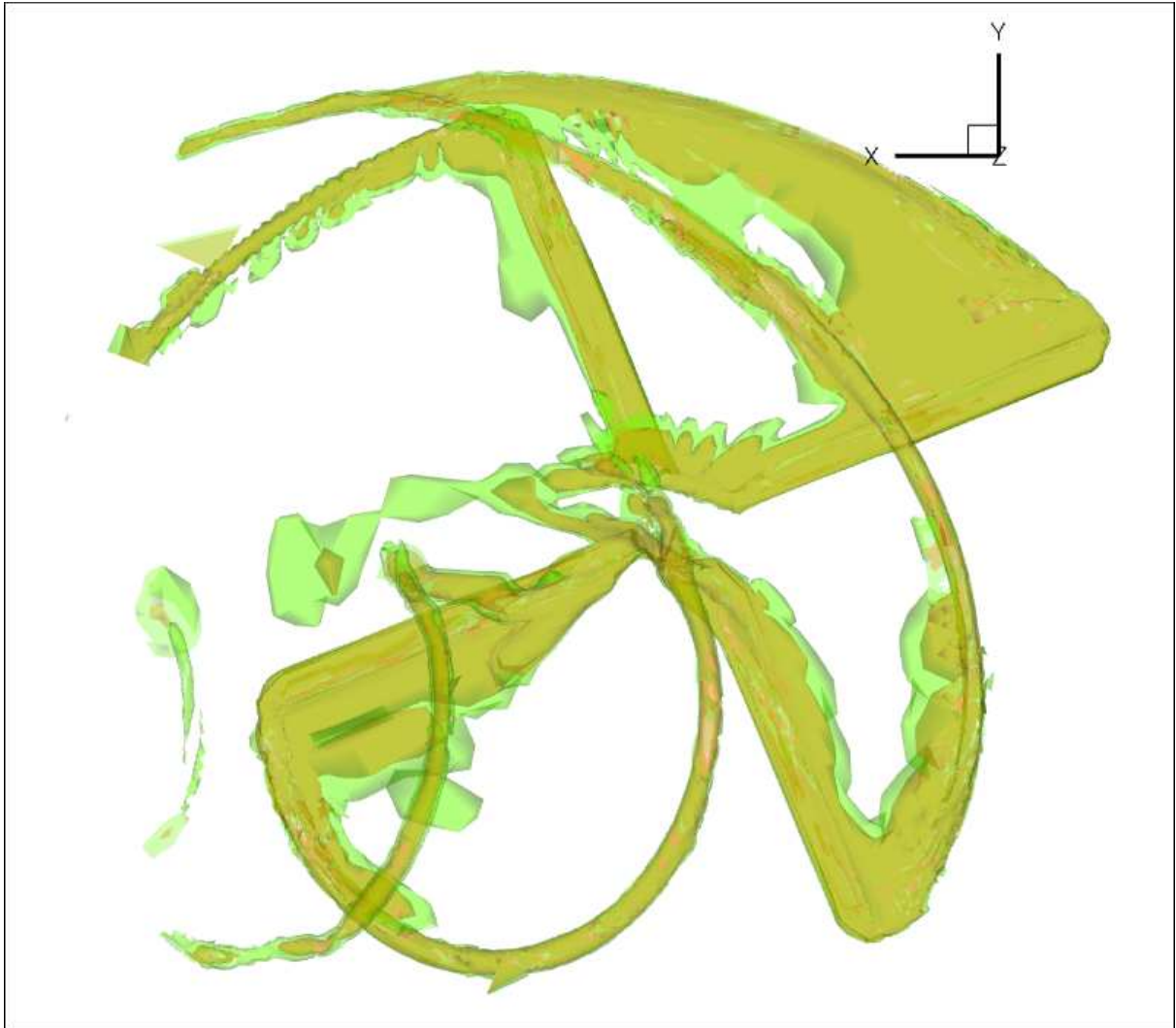
Figure 16 The vortex system at ψ=56°, as obtained with the third order method, viewed from below. Iso-contours are shown at vorticity magnitude level of 1.75a$_\infty$/R and 1.25a$_\infty$/R, where a$_\infty$ is the speed of sound.
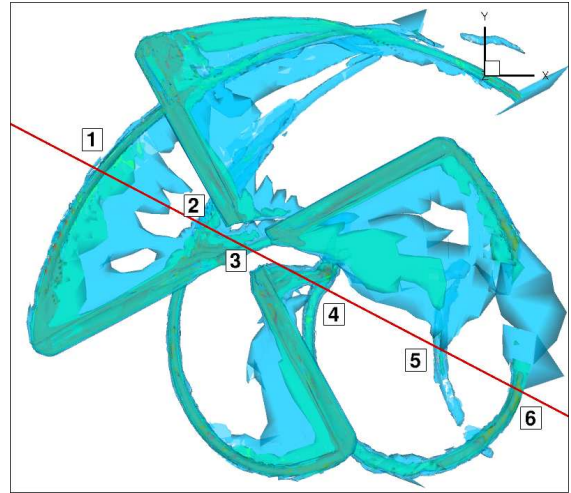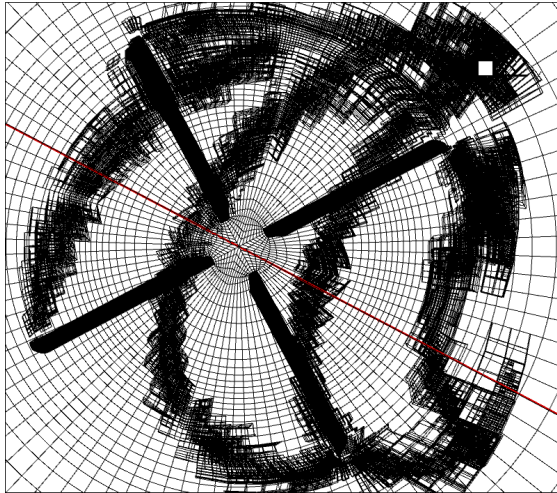
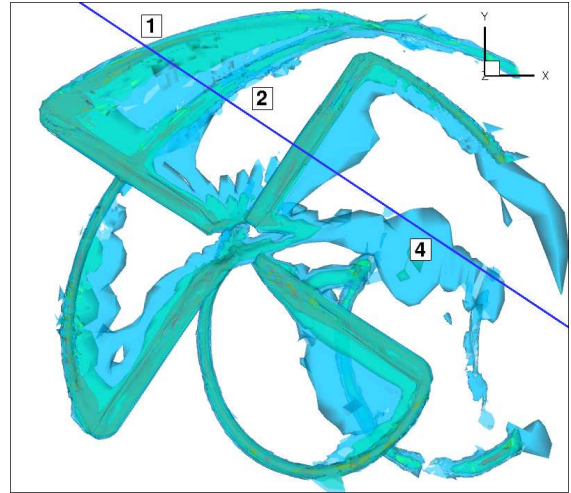*Figure 17 Definition of cross-section slice, shown in red, at ψ=28°*

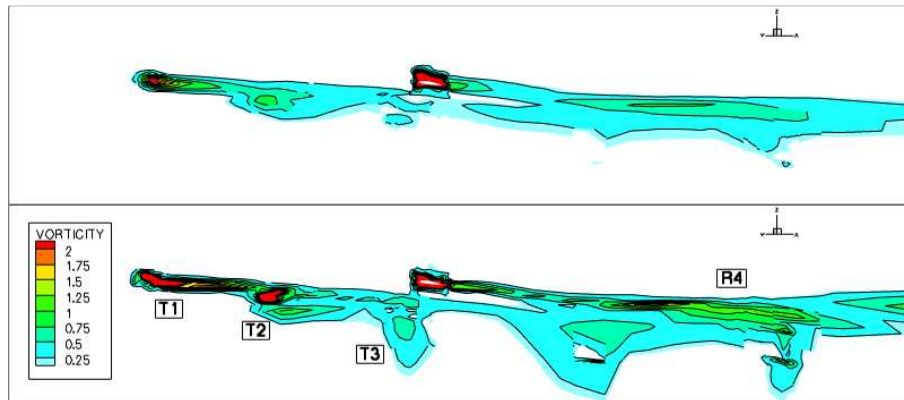*Figure 18 Vortex system at ψ=28°*
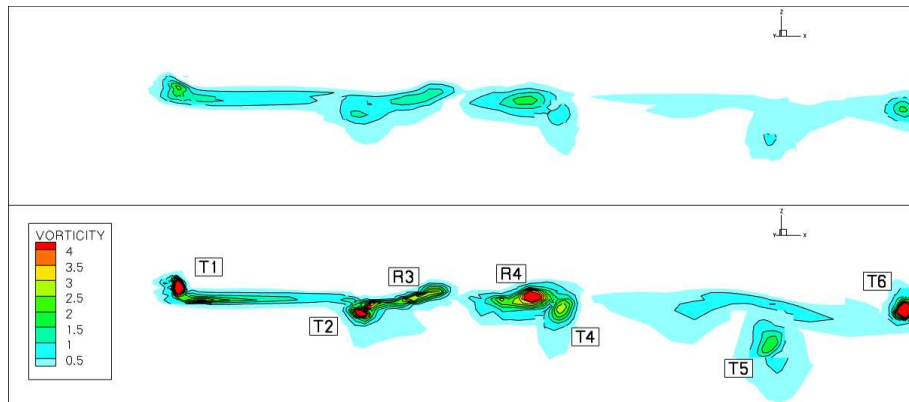
Figure 19 Comparison of vortex resolution in the slice defined in Figure 17 with second order simulation (top) and third order simulation (bottom)
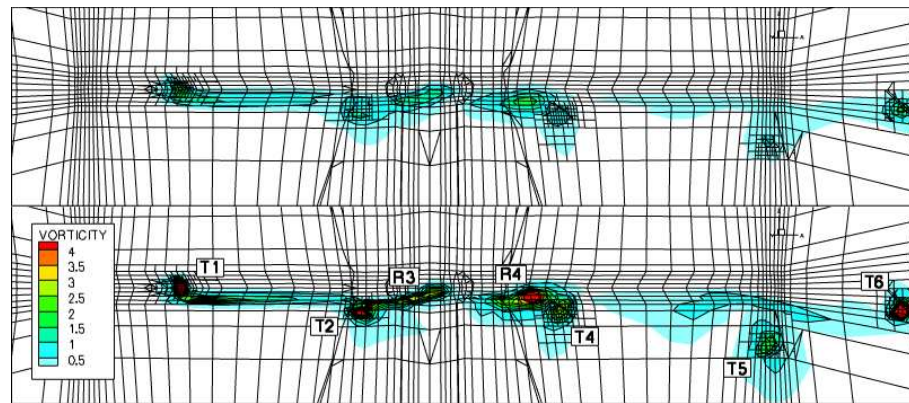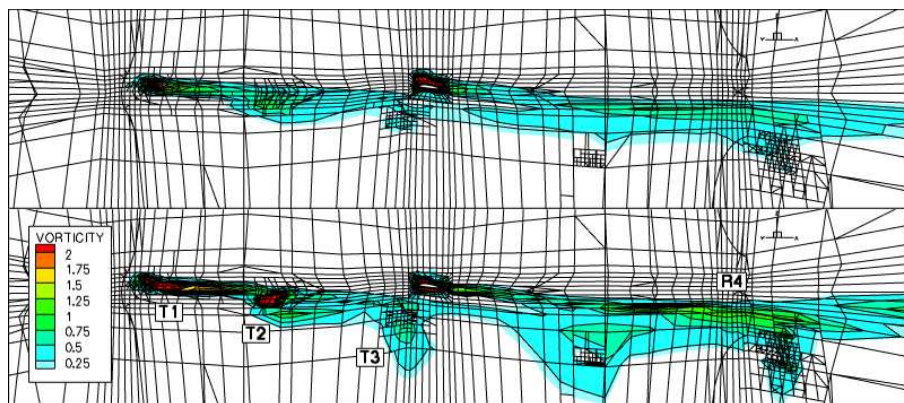

Figure 20 Comparison of vortex location in the slice defined in Figure 17 for second order (top) and third order simulation (bottom)
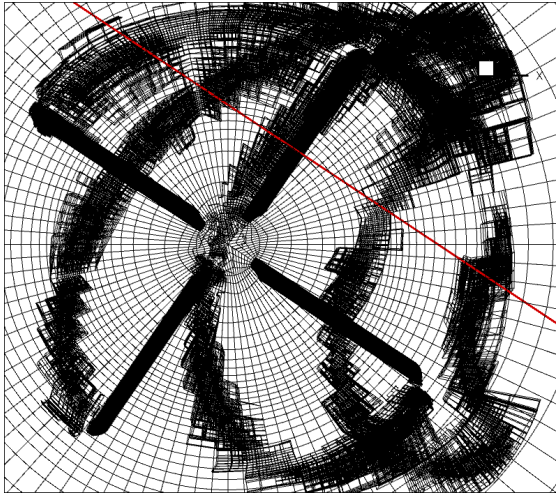
Figure 21 Definition of cross-section slice, shown in red, at ψ=56°

Figure 22 Vortex system at ψ=56°

Figure 23 Comparison of vortex resolution in the slice defined in Figure 21 with second order simulation (top) and third order simulation (bottom)

Figure 24 Comparison of vortex resolution in the slice defined in Figure 21 with second order simulation (top) and third order simulation (bottom). All cells are hexahedra, apparently triangular elements are a plotting anamoly.
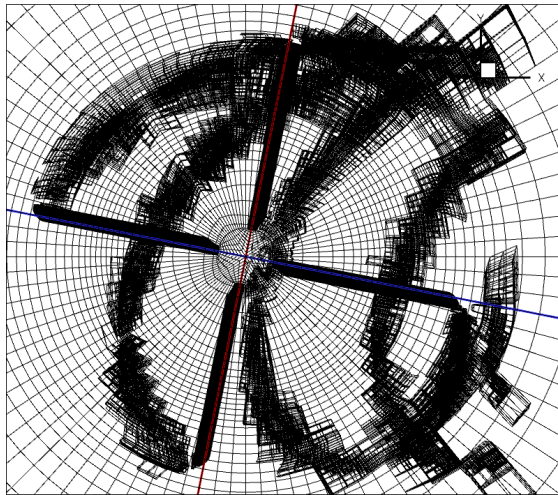
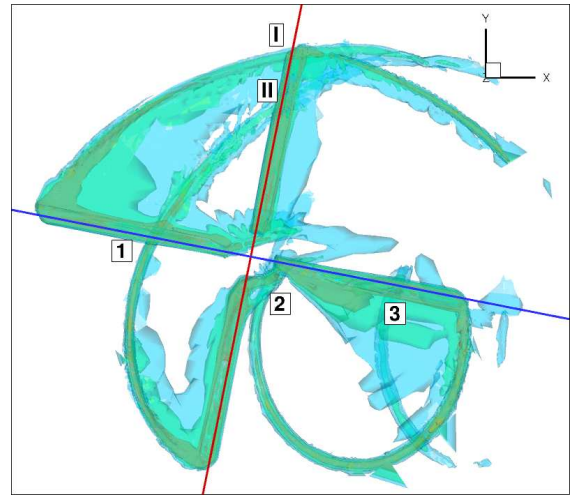Figure 25 Definition of cross-section slices, shown in red and blue, at ψ=80°
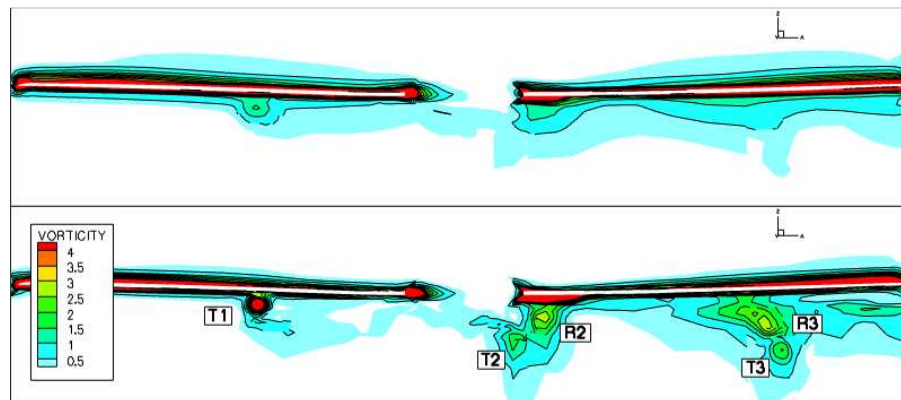
Figure 26 Vortex system at ψ=80°

Figure 27 Comparison of vortex resolution in the slice defined in Figure 25 by the blue line with second order simulation (top) and third order simulation (bottom). Flow is more or less from left to right.
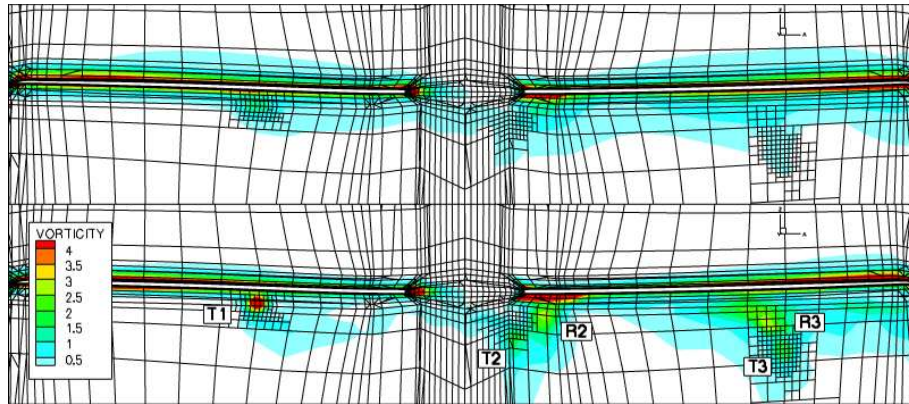
Figure 28 Comparison of vortex resolution in the slice defined in Figure 25 by the blue line with second order simulation (top) and third order simulation (bottom). Flow is more or less from left to right.
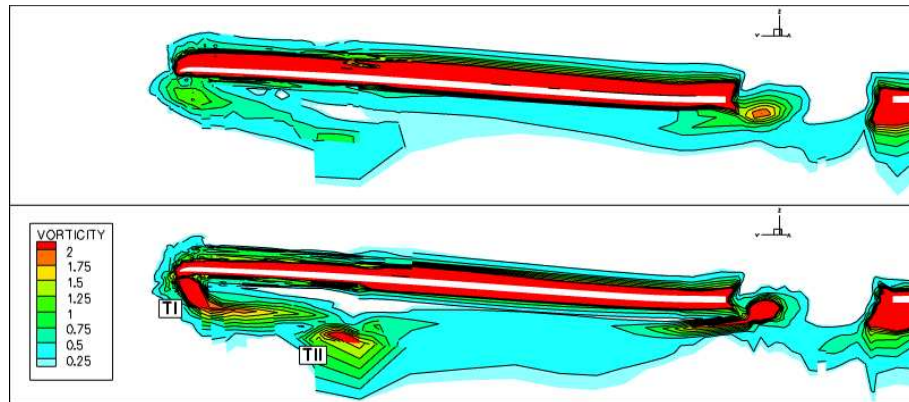

Figure 29 Comparison of vortex resolution in the slice defined in Figure 25 by the red line with second order simulation (top) and third order simulation (bottom).Flow is more or less perpendicular to the plane shown.
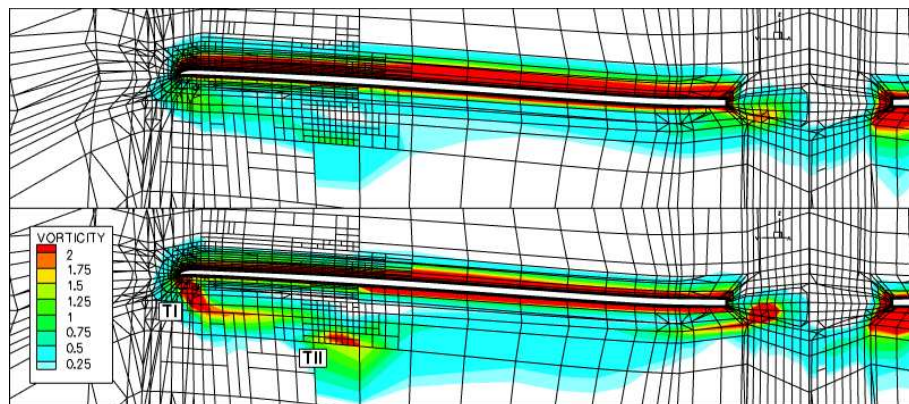

Figure 30 Comparison of vortex resolution in the slice defined in Figure 25 by the red line with second order simulation (top) and third order simulation (bottom).Flow is more or less perpendicular to the plane shown.

References

[1] O.J. Boelens, H. van der Ven, B. Oskam, and A.A. Hassan. Boundary conforming discontinuous Galerkin finite element approach for rotorcraft simulations. *J. of Aircraft*, **39** (5):776–785, Sep-Oct 2002.

[2] F.X. Caradonna, Development and challenges in rotorcraft aerodynamics, AIAA-2000-0109, 2000.

[3] A.T. Conlisk, The fluid dynamics of rotor wakes: theory, computation and experiment. AIAA 1999-3421, 1999.

[4] A. Datta, M. Nixon, and I. Chopra. Review of rotor loads prediction with the emergence of rotorcraft CFD. *J. American Helicopter Society,* **52**(4): 287-317, 2007.

[5] M. Dietz, E. Kramer, and S. Wagner, Tip vortex conservation using on a main rotor in slow descent flight using vortex-adapted Chimera grids, AIAA-2006-3478, 2006.

[6] N. Hariharan and L.N. Sankar. High-order essentially nonoscillatory schemes for rotary-wing wake computations. *J. of Aircraft,* **41**(2): 258-267, 2004.

[7] J. Jeong and F. Hussain, On the identification of a vortex, *J. Fluid Mech.*, **285**, 69-94, 1995.

[8] Norbert Kroll, ADIGMA – A European project on the development of adaptive higher order variational methods for aerospace applications, ECCOMAS CFD 2006, Egmond aan Zee, 2006.

[9] J. W. Lim, R. C. Strawn, Prediction of HART II rotor BVI loading and wake system using CFD/CSD loose coupling, AIAA paper 2007-1281.

[10] W. J. McCroskey, Vortex wakes of rotorcraft, AIAA 95-0530, 1995

[11] Mark Potsdam, Hyeonsoo Yeo, and Wayne Johnson, Rotor Airloads Prediction Using Loose Aerodynamic/Structural Coupling*, J. of Aircraft*, **43** (3), 2006.

[12] K.-J. Schultz, W. Splettstoesser, B. Junker, W. Wagner, E. Schoell, G. Arnaud, E. Mercker, K. Pengel, D. Fertis, A parametric wind tunnel test on rotorcraft aerodynamics and aeroacoustics (HELISHAPE) – Test Documentation and Representative results, DLR-IB-129-96/25, July 1996.

[13] R. Steijl, G.N. Barakos, and K.J. Badcock, Computational study of the advancing-side lift-phase problem, *J. of Aircraft,* **45** (**1**), 246-257, 2008.

[14] J.J.W. van der Vegt and H. van der Ven, Space-time discontinuous Galerkin finite element method with dynamic grid motion for inviscid compressible flows. Part I. General formulation. *J. of Comp. Physics*, **182**, 546-585, 2002.

[15] H. van der Ven and O.J. Boelens. Towards affordable CFD simulations of rotor in forward flight – a feasibility study with future application to vibrational analysis. In *proceedings of the 59th American Helicopter Society Forum, Phoenix, Arizona, USA, May 6-8, 2003*, 2003.

[16] H. van der Ven and O.J. Boelens. A framework for aeroelastic simulations of trimmed rotor systems in forward flight. In *proceedings of the 30th European Rotorcraft F*orum, *Marseille, September 14-16, 2004*, 2004.

[17] H. van der Ven, An adaptive multitime multigrid algorithm for time-periodic flow simulations, *J. of Comp. Physics*, **227**, 5286-5303, 2008.